

Realistic computer models of amorphous $\text{ZrO}_2\text{:Ta}_2\text{O}_5$: Structural, optical, and vibrational properties

Rajendra Thapa^{1,*}, Kiran Prasai,² Riccardo Bassiri², Martin M. Fejer,² and D. A. Drabold^{3,†}

¹*Department of Physics and Astronomy, Nanoscale and Quantum Phenomena Institute (NQPI),
Ohio University, Athens, Ohio 45701, USA*

²*Edward L. Ginzton Laboratory, Stanford University, Stanford, California 94305, USA*

³*Department of Physics and Astronomy, Ohio University, Athens, Ohio 45701, USA*



(Received 22 December 2021; accepted 10 June 2022; published 27 June 2022)

Amorphous zirconia-alloyed-tantala ($\text{ZrO}_2\text{:Ta}_2\text{O}_5$) is of interest as a prospective coating material to make the highly reflective mirrors used in gravitational wave detectors. We study the atomic structure of thin films of $\text{ZrO}_2\text{:Ta}_2\text{O}_5$ by making realistic computer models using force enhanced atomic refinement. The models are, by construction, in agreement with measured x-ray scattering functions. The models made with x-ray scattering data on as-deposited and 800 °C-annealed samples showed clear structural differences, particularly in their metal-metal correlation. The ratio of corner-shared to edge-shared polyhedra increased as a result of annealing. The electronic band gap and the density of states of $\text{ZrO}_2\text{:Ta}_2\text{O}_5$ are found to be similar to that of pure Ta_2O_5 and remained unchanged upon annealing. We used the Hyed-Scuseria-Ernzerhof hybrid functional to estimate the band gap of $\text{ZrO}_2\text{:Ta}_2\text{O}_5$ to be ≈ 4 eV, which is close to the experimental band gap of pure Ta_2O_5 . The refractive indexes calculated from the models were in reasonable agreement with the experiment. Vibrational modes at high frequencies involve highly localized bond stretch modes associated with a corner-shared O atom connecting two metal-oxygen polyhedra.

DOI: [10.1103/PhysRevB.105.224207](https://doi.org/10.1103/PhysRevB.105.224207)

I. INTRODUCTION

The sensitivity of interferometric gravitational wave detectors such as LIGO and Virgo can be limited by Brownian thermal noise associated with the dielectric coatings that make up the highly reflective mirrors used in the interferometer [1–3]. These coatings consist of alternating layers of high and low refractive index materials. In the current generation of LIGO and Virgo, silica (SiO_2) is the low index material and titania-doped tantala ($\text{TiO}_2\text{:Ta}_2\text{O}_5$) is the high index material [3]. The measured mechanical loss angle for the state-of-the-art ion-beam-sputtered SiO_2 coatings is 4×10^{-5} rad [4,5] while that for $\text{TiO}_2\text{:Ta}_2\text{O}_5$ is 2.4×10^{-4} rad [6,7]. Hence, the dominant contributor to the coating thermal noise is high index $\text{TiO}_2\text{:Ta}_2\text{O}_5$ layer. One of the ways of reducing coating thermal noise and increasing the sensitivity of future upgrades of these detectors is to find a low-mechanical-loss replacement for the high-index layer.

Zirconia-alloyed tantala ($\text{ZrO}_2\text{:Ta}_2\text{O}_5$) has been studied as a promising candidate to replace the high index layer [1,3]. In addition to having a higher refractive index (>2 at 1064 nm) compared to silica (1.45 at 1064 nm), $\text{ZrO}_2\text{:Ta}_2\text{O}_5$ appears to remain amorphous after annealing up to temperatures of 800 °C while most other Ta_2O_5 -based coatings could be annealed without crystallization only up to 600 °C. This is significant because postdeposition annealing is a standard procedure to reduce room-temperature (RT) mechanical loss of

amorphous oxide coatings. Measurements have shown this to be true for $\text{ZrO}_2\text{:Ta}_2\text{O}_5$ as well—measured values of RT loss are seen to decrease monotonically as these coatings are subjected to higher and higher annealing temperatures before the crystallization starts [1]. Since annealing the low index layer SiO_2 also drives down its mechanical loss, this recipe could form a potential route to low thermal noise high-reflection coating.

To understand the origin of mechanical loss in the thin films of $\text{ZrO}_2\text{:Ta}_2\text{O}_5$ and possibly find ways to reduce the loss, it is important to study its atomic structure and the ways two-level systems (TLSs), which are thought to be responsible for loss processes, could form in its structure. Furthermore, since the RT mechanical loss values of $\text{ZrO}_2\text{:Ta}_2\text{O}_5$ continuously decrease upon annealing [1], it could be especially informative to probe the annealing-induced effects on its atomic structure and how those changes in atomic structure might relate to an observed decrease in RT mechanical loss.

In an earlier work published by Prasai *et al.* [3], x-ray grazing incidence pair distribution function (GIPDF) measurements carried out on differently annealed thin films of $\text{ZrO}_2\text{:Ta}_2\text{O}_5$ are reported. These measurements are then employed to generate structural models of $\text{ZrO}_2\text{:Ta}_2\text{O}_5$. Generating several sets of models based on GIPDFs measured on differently annealed samples allowed the study of annealing-induced effects on atomic structure. The modeling method employed in this work is force-enhanced atomic refinement (FEAR) [8,9]. FEAR uses force-based energy minimization to constrain the solution space of reverse Monte Carlo (RMC) modeling so the resulting models are simultaneously in agreement with scattering data as well as low-energy configurations

*rt887917@ohio.edu

†drabold@ohio.edu

respecting the chemical and topological order required by the chosen force field.

In this paper, we revisit the atomic modeling part of Ref. [3] employing density functional theory (DFT)-based calculations for energy minimization instead of two-body empirical forcefield used in Ref. [3]. We gain significant accuracy in modeled atomic interactions by using DFT-based calculations compared to the simple two-body empirical forcefields. Furthermore, electronic and optical properties of the models could be calculated using the DFT-based calculations. However, the size and number of instances we could model the system are significantly limited in the present work compared to Ref. [3] and hence our ability to resolve small differences between differently annealed systems is poorer in the present paper compared to Ref. [3]. Based on the models we generate, we report on several characteristics, including coordinations, polyhedral connections, bond angle distribution, voids, electronic and phonon density of states (DOS), and refractive index. The optical properties are of special interest to LIGO and VIRGO applications.

The rest of the paper is organized as follows: Section II includes discussions about computational methodology and models, Sec. III outlines the results and discussion, and Sec. IV summarizes our conclusions and indicates future research directions.

II. METHODOLOGY AND MODELS

We prepare 416-atom FEAR [8,9] models at experimental density (6.53 g/cc) [3]. Atomic coordinates from a well-equilibrated melt from a building block [10] model (cooling rate of 0.1 K/fs) at 4000 K was taken as the starting model. This configuration was then refined iteratively with partial RMC [11] and energy minimization carried out with conjugate gradient algorithm using the *ab initio* plane-wave DFT theory package VASP [12] with the projector augmented wave (PAW) [13] method and the Perdew-Burke-Ernzerhof (PBE) [14] treatment of the exchange-correlation functional. The *ab initio* minimization step in each FEAR iteration ensures that the interactions and chemistry are well represented, and the system does not produce chemically unrealistic structures which usually arise from conventional RMC. This process was repeated to produce five independent models with each of the annealed and as-deposited data, and the energy per atom on various models were within 2% of the average value. Each model, after the FEAR convergence, were relaxed with conjugate gradient relaxation in VASP until the system attains a DFT minimum of energy. After this relaxation, the final energies per atom in the as-deposited and annealed models were almost the same. In particular, it would be interesting to get a measure of the difference between as-deposited and annealed models fitted to the two experimental results.

For validation and comparison purposes, we created a melt quench (MQ) model of $\text{ZrO}_2:\text{Ta}_2\text{O}_5$ with 312 atoms. The final force/energy relaxed model showed weaker agreement with the experimental data for as-deposited films compared to the FEAR models. Since creating models of as deposited and annealed $\text{ZrO}_2:\text{Ta}_2\text{O}_5$ is rather complicated with traditional MQ, it would be difficult to study annealing induced changes with the MQ models. Although post-treatment of MQ

models to model annealing effects have been established and tested [15,16], FEAR seems to be the go-to direction for our material.

Furthermore, an x-ray scattering amplitude from a sample depends on the atomic number of the species present [17], therefore being less sensitive to O atoms relative to the Zr and Ta atoms. RMC alone with x-ray diffraction data could thus result in unexpected O behavior in such O rich stoichiometry. This shortcoming could be ameliorated by a FEAR simulation technique, where accurate interatomic potentials for each atomic species are used to refine the models.

The electronic structure of the models have been studied, in addition to the usual PBE functional, using the Heyd, Scuseria, and Ernzerhof (HSE06) hybrid functional [18–20], which has been quite successful in handling the DFT band-gap problem and predicting optical properties. In this class of hybrid functional, the exchange potential is divided into short- and long-range parts. For our system, we used the standard screening parameter ($\omega = 0.2$), with ω being related to the characteristic length, $2/\omega$, which defines the range separation. We have used default mixing parameters: 25% of the nonlocal Hartree-Fock exchange is mixed with 75% of the semilocal exchange in the generalized-gradient approximation of PBE [14]. The long-range part and the correlation are determined using PBE. Also the ion-core and valence electron interactions were calculated with the PAW potentials.

III. RESULTS AND DISCUSSION

A. Structural properties

The structure factor $S(Q)$ and the pair distribution function (PDF) obtained from the models are shown in Fig. 1, along with the experimental data for comparison. The results were averaged over five independent models for both the as-deposited and annealed data. Both as-deposited and annealed models agree reasonably well with the experiment. The PDF of both as-deposited and annealed models show amorphous nature indicating that $\text{ZrO}_2:\text{Ta}_2\text{O}_5$ does not crystallize upon 800 °C annealing. As previously reported, this phenomena arises due to the competing structural phases of zirconia interfering with the alignment of tantala polyhedra and thereby suppressing crystallization without generating a separate zirconia crystalline phase [21]. Additionally, Tewg *et al.* has also reported a 200 °C increase in the amorphous-to-polycrystalline transition temperature of tantala with the right amount of zirconia doping [21].

To understand the annealing-induced changes in the structure, we plot the $S(Q)$ and $G(r)$ of as-deposited and annealed models together with the difference between them in Fig. 2. The differences in $S(Q)$ are prominent at the first and second peaks while the differences in $G(r)$ manifest mostly in the region between 3 Å–4 Å. This region of $G(r)$ carries information regarding the connection of the various metal-oxygen polyhedra and therefore the figure suggests that annealing produces significant changes in these connections. The difference between the as-deposited and annealed models are subtle, and it is difficult to reliably pinpoint the differences in our models because the effects are so small. However, we calculated the standard error arising from the averaging over five models and

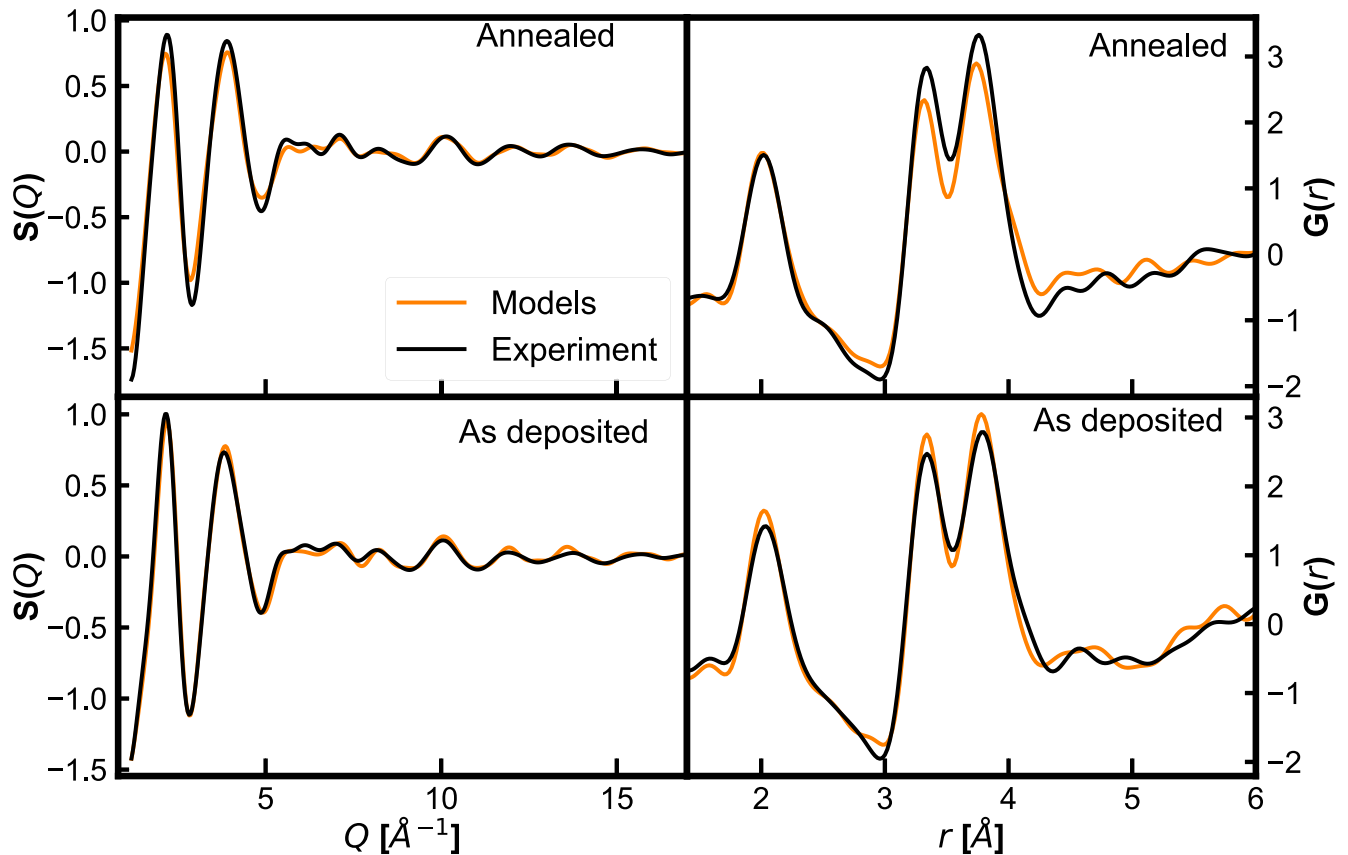


FIG. 1. Comparison of models with experiment: Experimental $S(Q)$ and $G(r)$ compared with that obtained from the models. The results are averaged over five models.

verified that the differences in the $G(r)$ and $S(Q)$ between the as-deposited and annealed models were higher than the error.

To understand the real-space correlations of the atoms, the structure of the material can be thought of as a collection of metal atom centered polyhedra with O atoms at the corners. The correlation between the metal and the O atoms within a polyhedra give rise to the first peak in $G(r)$ at 2 Å. Metal-metal (M–M) correlations arising from different types of connections between the polyhedra, shown in Fig. 3 (left panel), give peaks in $G(r)$ at different distances: edge-shared (ES) and face-shared (FS) connections combined show up as a peak at 3.5 Å while corner-shared (CS) connections give rise to a peak at 3.80 Å. These findings are in good agreement with similar calculations made previously on zirconia-alloyed tantalum [3] and on pure tantalum [22,23].

Figure 3 (left panel) presents a comparison of $G(r)$ from as-deposited and annealed models, with the lines thickened to show standard errors. It shows that the M–O correlation is robust and unaltered by annealing. Low values of standard errors below 3 Å in both as-deposited and annealed models show that all the models taken for averaging purposes had almost the same M–O correlation in them. The M–M correlations, however, are modified significantly as a result of annealing. Annealed models tend to have a larger concentration of CS polyhedra and a lower concentration of FS polyhedra compared to the as-deposited models. The comparison of different polyhedral connection are shown on the right panel of Fig. 3, suggesting that annealing increases the number of CS connec-

tions while decreasing the ES and FS connections between metal atoms in the network. As the measured RT mechanical loss of these thin films decrease upon annealing [3], this result supports the notion that TLSs contributing to the RT mechanical loss may involve ES and FS connections.

The bond angle distribution function obtained from the models is shown in Fig. 4. The most obvious change in the bond angle occurs in the Ta–O–Ta connections. This increase in the peak around 130° for the annealed model is due to the increase in the CS Ta–Ta connections upon annealing. This finding has already been pointed out in our earlier work [3].

The coordination statistics of each atomic species are summarized in Table I. The bond cutoffs were taken from the first

TABLE I. Coordination statistics for as-deposited and annealed models using 2.9 Å M–O bond cutoff distance along with the fluctuations in the total coordination number over different models.

Model	Atoms	Ta	O	Zr	Total
As deposited	Ta		6.07		6.069 ± 0.038
	O	1.35		1.41	2.759 ± 0.003
	Zr		6.35		6.346 ± 0.031
Annealed	Ta		5.90		5.896 ± 0.031
	O	1.31		1.41	2.718 ± 0.007
	Zr		6.34		6.342 ± 0.053

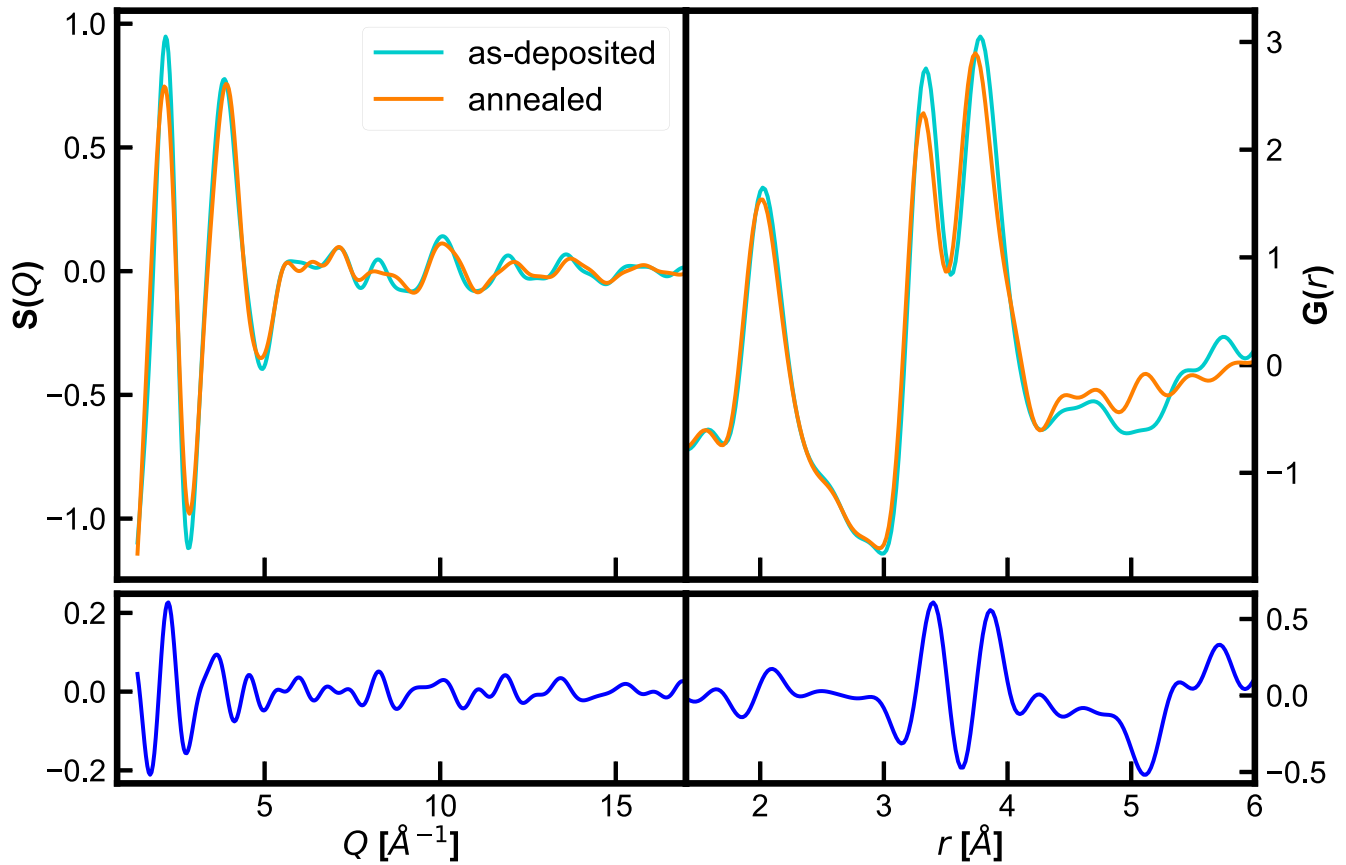


FIG. 2. Comparison of as-deposited and annealed models: Comparison of $S(Q)$ and $G(r)$ from as-deposited and annealed models. The difference curve has been shown at the bottom.

minima of the PDF and the coordination statistics are not too sensitive to this choice. Homopolar bonds are absent in all the as-deposited as well as annealed models and the only bonds present are the M–O bonds. The Ta–O coordination values for the as-deposited and annealed models are in agreement with results from NMR studies on pure Ta₂O₅ [24,25]. Annealing did not produce a major change in the Zr–O coordination number but the Ta–O was significantly reduced as a result of

annealing causing a major reduction in the O–Ta coordination number and the average O coordination by metal. As seen in Fig. 5, this reduction in O–M coordination number arises from a drop in fraction of three- and four-coordinated O atoms as a result of annealing. This finding is complemented by an increase in fivefold Ta-atom due to annealing. Reduction in O coordination by metal upon annealing has previously been reported in similar measurements [3]. A significant change

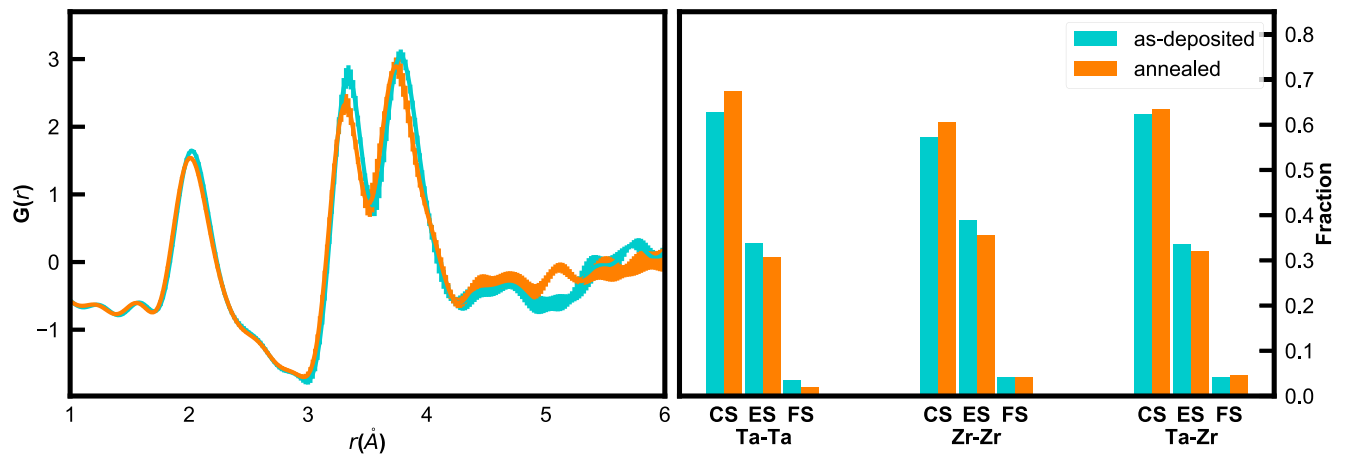


FIG. 3. Effect of annealing in M–M correlation and polyhedra sharing fashion. Left panel: Comparison of $G(r)$ from as-deposited and annealed models. The curves are thickened to show the standard error present in the data. Right panel: Comparison of the fraction of CS, ES, and FS polyhedra connections in the as-deposited and annealed models.

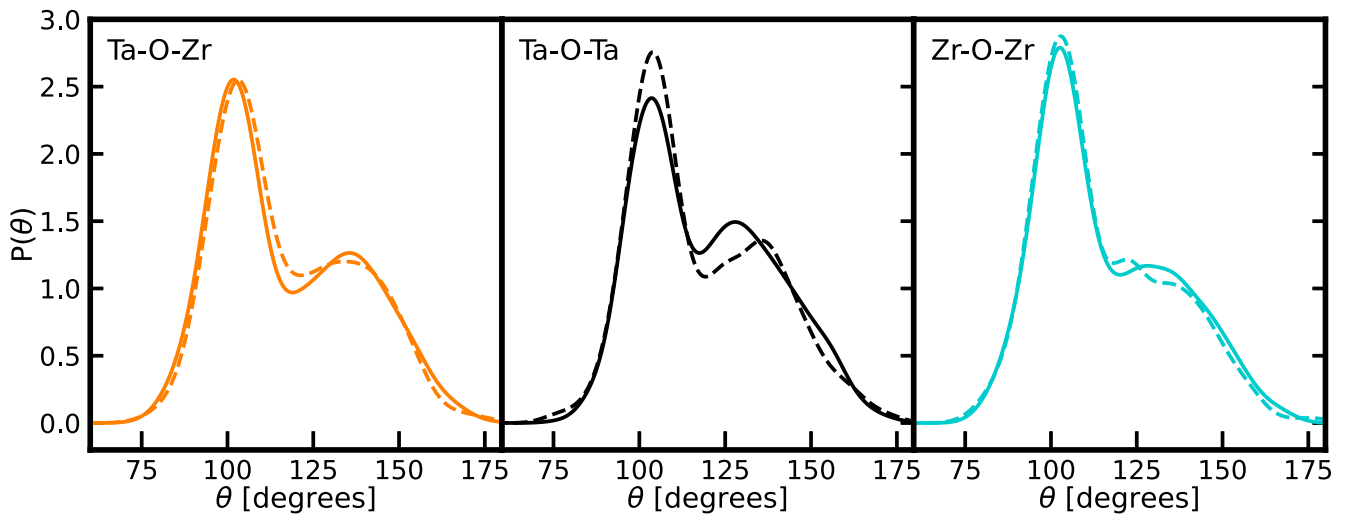


FIG. 4. Bond angle distribution function for the as-deposited (dashed line) and annealed model (solid lines).

in Ta–O coordination compared to Zr–O upon annealing suggests that the Zr–O ionic bond is stronger than Ta–O, a fact also backed up by their electronegativity values. The ratio of twofold to threefold coordinated O atoms in zirconia-alloyed tantalum is $\sim 1 : 2$. Thus, zirconia doping modifies the bonding environment of oxygen significantly by producing more threefold coordinated O atoms in the network. Figure 5 also shows that annealing reduces the fraction of higher coordinations across each species.

1. Voronoi analysis

The local environment around each atom is studied with Voronoi analysis. A Voronoi tessellation is defined by associating a cell of space to each atom that is closer to that atom than any other [26]. In general, a Voronoi cell for an atom can be constructed by drawing perpendicular bisector planes between the atom and its near neighbors.

The Voronoi radius (VR) for an atom can be obtained from the cell volume within the atomic sphere approximation that approximates the cell with a sphere equal to its volume. With this construction, atoms with closer neighbors distributed symmetrically have smaller VR while atoms with neighbors further away have larger VR. Furthermore, if an atom has a void near it, the Voronoi volume and hence the

radius is higher. Distribution of the VR in the sample has been shown in Fig. 6. The peak arising from Ta atoms is a clear signature of the Ta–O bonds because it is the shortest bond present in the network. The decrease in the peak height for Ta atoms upon annealing is a consequence of decrease in the O–Ta coordination. Since the range for the VR for Ta atoms is the smallest, the Ta atoms have the most compact nearest-neighbor environment. Detailed analysis of the bonding environment showed that the tail of the Ta atoms are contributed by undercoordinated (fivefold) Ta atoms while the lower end is contributed by overcoordinated Ta atoms. Another peak due to Zr atoms lies in the intermediate region of O and Ta atoms because the bond length of Zr–O bonds is greater than that for Ta–O [3]. Low values of VR for both Zr and Ta atoms compared to O atoms highlight two key structural details of the models. First, the environment around metal atoms are more organized than the O atoms as most metal atoms have a M–O polyhedral environment. Second, there is always an O atom closer to a void than any metal atoms. The VR associated with the oxygen atoms are the largest among the three which can be attributed to various factors. First, O atoms have the smallest number of nearest neighbors with no clear three-dimensional picture of its environment: its neighbors are not arranged symmetrically. Second, they lie

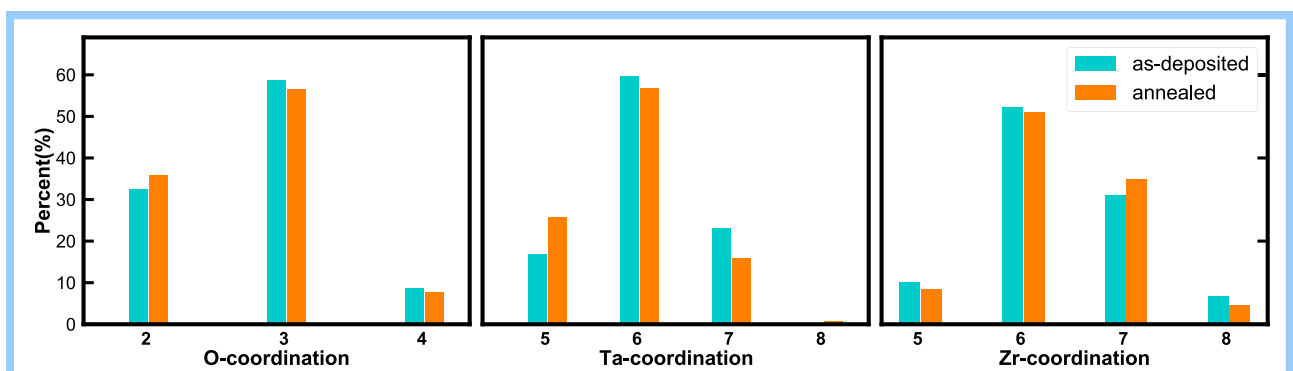


FIG. 5. Change in coordination accruing from annealing.

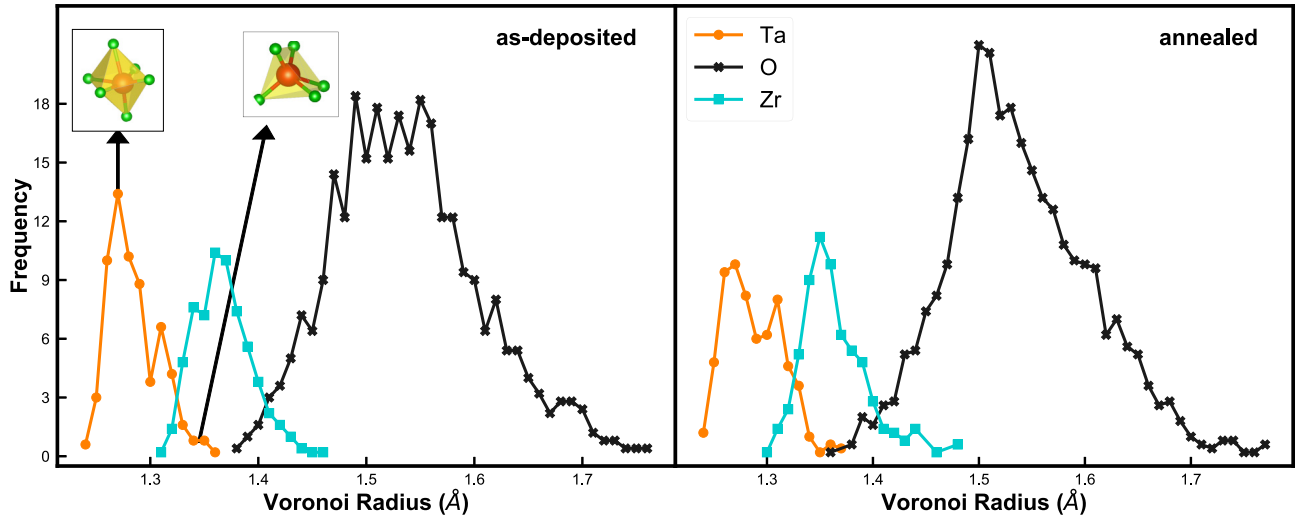


FIG. 6. Frequency distribution of Voronoi radius. The sum of the frequencies for each atom type is equal to the number of atoms of that particular type in the sample. The jagged oscillations are artifacts of the model size.

in the boundary separating voids and the dense matrix of atoms and have large unoccupied volumes included in their Voronoi cells.

2. Voids

We begin by partitioning the system into a large number of small spherical cells centered at the points of a $180 \times 180 \times 180$ grid and checking the distance of each sphere from all the atoms in the network. A cell is called isolated if it is further away than the covalent radius (1.70 Å for Ta, 0.73 Å for O, and 1.75 Å for Zr), plus a tolerance, from all the atoms in the network. We have used a tolerance of 0.9 Å to get rid of the inclusion of the cells lying along the M–O bonds, with a 2.90 Å cutoff, in the set of isolated cells. The collection of these isolated cells defines the region in real space in the network that is empty/void. We define void size as the combined volume of all the isolated cells within a void. The void sizes in the models are presented in Fig. 7. The fluctuations of void sizes among various models were within a few percent of the void size. The distribution of the void size shows that the as-deposited models, on average, have larger voids than the annealed models. The annealed models have a few large voids and a higher fraction of uniformly sized

smaller voids. Annealing thus annihilates the larger voids into smaller sizes which can be thought of as the bonded O atoms being pushed further from the metal atom, thereby reducing the coordination, although subtly, as shown in Table I. This fact is also corroborated by the decrease in the fraction of highest coordinated metal atoms upon annealing, as seen in Fig. 5, which can be thought of as the O atom being pushed toward the void, thereby annihilating the void. This is true not just for the 312-atom models but also for 2600-atom model.

For visual interpretations, the voids present in one of the as-deposited and annealed FEAR models are shown in Fig. 8. It shows that voids in the annealed sample are uniformly distributed and with a narrower range of sizes than the as-deposited models.

B. Optical and electronic properties

The frequency-dependent complex dielectric function,

$$\epsilon(\omega) = \epsilon_1(\omega) + i\epsilon_2(\omega), \quad (1)$$

for the as-deposited and annealed models were calculated within the PAW method, where the imaginary part is derived by summing over conduction bands and the real part using the Kramers-Kronig relation [27]. Both refraction and absorption

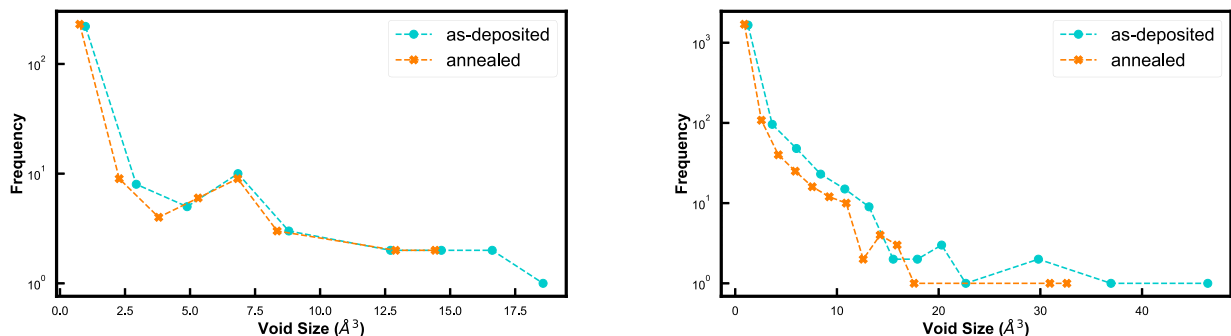


FIG. 7. Void size in the 416-atom (left) and 2600-atom (right) models. Both show annihilation of the voids upon annealing.

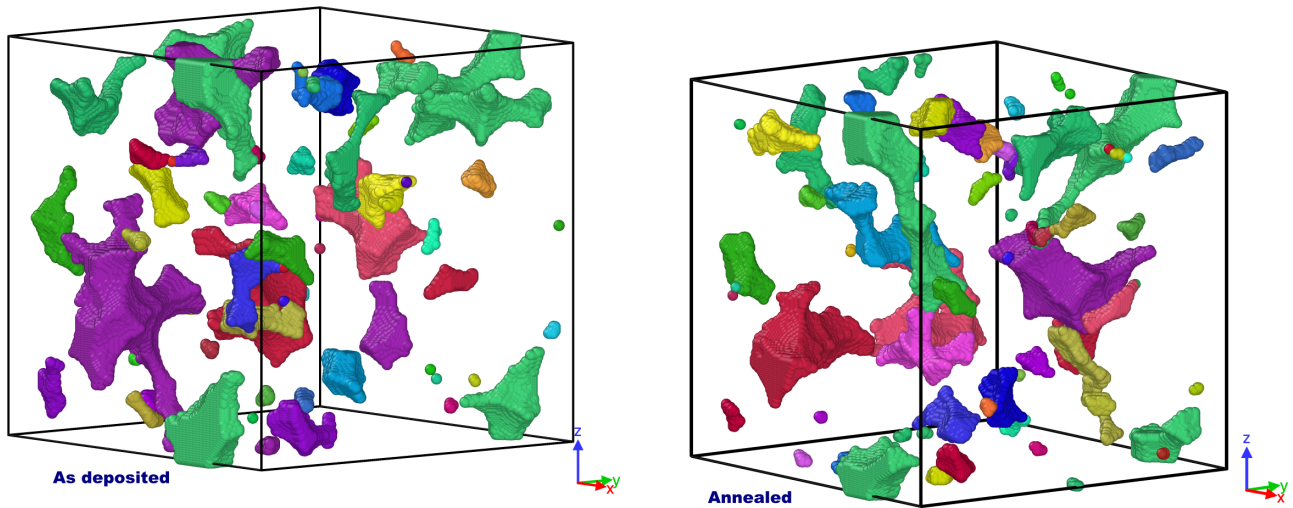


FIG. 8. Distribution of voids in real space for as-deposited and annealed models. Different colors denote different voids in the system.

of a medium can be described by a single quantity called complex refractive index defined as

$$\tilde{n} = n + ik. \tag{2}$$

The real part is the normal refractive index while the imaginary part is called the extinction coefficient and is directly proportional to the absorption coefficient of the medium. Both quantities are calculated using the complex dielectric function with these definitions [28]:

$$n = \left(\frac{\sqrt{\epsilon_1^2 + \epsilon_2^2 + \epsilon_1}}{2} \right)^{\frac{1}{2}}, \quad k = \left(\frac{\sqrt{\epsilon_1^2 + \epsilon_2^2 - \epsilon_1}}{2} \right)^{\frac{1}{2}}. \tag{3}$$

The frequency dependence of the refractive index, calculated with the PBE and HSE06 functionals, has been shown in

Fig. 9. The refractive index for both as-deposited and annealed models, obtained using the hybrid functional (HSE-06), were much closer to the experimental results. The experimental value of the refractive index at 1064 nm is reported to be 2.08 ± 0.01 [1]. From Fig. 9, the value calculated with HSE is much closer to the experimental value compared to that calculated with PBE.

The electronic density of states of the models evaluated with the Kohn-Sham eigenfunctions obtained from VASP using PBE and the HSE06 hybrid functional have been plotted in Fig. 10. Since tantala is an insulator with a experimental band gap of 4.22 eV [29], introduction of zirconia (with band gap of 5.50 eV [30]) to the network does not change the insulating nature of the compound in contrast to the results seen in Cu-doped tantala [31], where space-projected conductivity calculations have shown that the phase-segregated Cu atoms

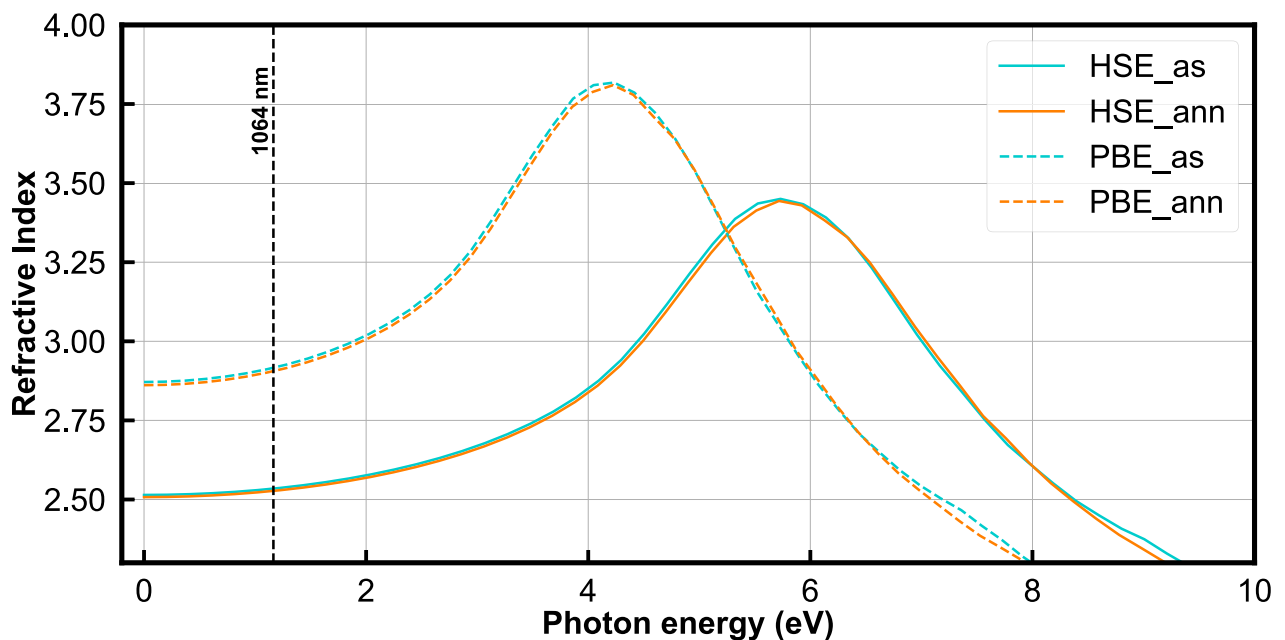


FIG. 9. Refractive index as a function of photon energy for as-deposited and annealed models.

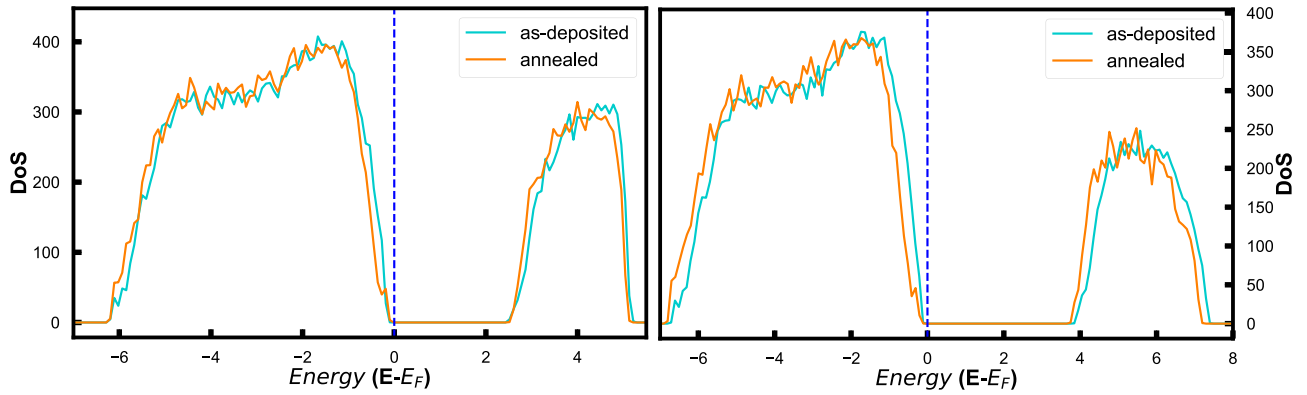


FIG. 10. Comparison of the electronic density of states (EDOS) between as-deposited and annealed models calculated using PBE (left panel) and HSE06 (right panel) approximations.

form a conducting active region. The band gap observed in our models (≈ 2.3 eV) calculated with the PBE approximation is lower than reported, a discrepancy which can be associated with the well-known band-gap underestimation by DFT [32]. However, the band gap calculated with the hybrid functional (HSE06) shows a band gap ≈ 4 eV which is close to the experimental band gap of tantala. The band gap for crystalline tantala and zirconia calculated using density-functional calculations have been reported to be 2.2 eV [33] and 5.34 eV [34], respectively. Figure 10 also shows that the gap in the DOS is robust with respect to annealing.

C. Vibrational properties

The analysis of the vibrational properties of amorphous materials not only serves as a tool to validate (or invalidate) computer generated models but also provide a useful insight to the local bonding environment. Vibrational properties of the models were studied using the harmonic approximation. The analysis begins with a zero-pressure relaxation of the models which resulted in a slight change in volume ($\sim 1\%$) with no significant changes in network topology. The Hessian matrix is then computed by displacing each atom in six directions ($\pm x, \pm y, \pm z$) by 0.015 \AA . The three lowest frequencies arising from rigid supercell transitions were removed from the calculations of the vibrational density of states (VDOS). The VDOS is defined as

$$g(\omega) = \frac{1}{3N} \sum_{i=1}^{3N} \delta(\omega - \omega_i), \quad (4)$$

with N and ω_i representing the number of atoms and the eigenfrequencies of normal modes, respectively. This mathematical definition suggests that any frequency that has a higher number of eigenfrequencies in its neighborhood will have higher VDOS. The delta function is approximated by a Gaussian with a standard deviation of $\sigma = 1.8 \text{ meV}$.

The extent of localization of the vibrational frequencies are studied using vibrational inverse participation ratio (VIPR) defined as

$$\mathcal{V}(\omega_n) = \frac{\sum_{i=1}^N |\mathbf{u}_n^i|^4}{\left(\sum_{i=1}^N |\mathbf{u}_n^i|^2\right)^2}, \quad (5)$$

where \mathbf{u}_n^i is displacement vector of i^{th} atom at normal mode frequency ω_n . Low values of VIPR indicate a vibrational mode evenly distributed among the atoms while higher values imply only a few atoms contributing at that particular eigenfrequency. This quantity helps us determine what atoms share the vibrational mode at any particular frequency.

The VDOS for the as-deposited and annealed models have been shown in Fig. 11. A detailed analysis of the contribution from individual atomic species showed the dominance of metal atoms at low frequencies while O atoms dominated the mid and high regions of the vibrational spectrum. The VDOS looks qualitatively similar in the as-deposited and the annealed models at low frequencies. However, there are certain regions where they differ significantly as we move higher in frequency, for example, near $\approx 57.5 \text{ meV}$. The insets show that the discrepancy arises because of the difference in the number of the vibrational modes present in the as-deposited and annealed models in that region.

The VIPR for the O atoms, decomposed onto different O coordinations, is plotted in Fig. 11. Low values of VIPR throughout the vibrational spectrum for the fourfold O atoms indicate that the vibrational eigenmodes these set of atoms contribute to are highly delocalized. The normal modes toward the higher end of the spectrum are mostly localized on the twofold O atoms and on the threefold O atoms to some degree. A detailed investigation of these localized high-frequency modes show that they are localized on a CS O atom connecting two M–O polyhedra and the vibrational mode is a bond stretch mode of the CS O atom between the two metal atoms. This localization at high frequency is important for thermal application because localized modes play a significant role in determining thermal conductivity in amorphous chalcogenides [35] and polymers [36].

IV. CONCLUSIONS

New models of both as-deposited and annealed $\text{ZrO}_2:\text{Ta}_2\text{O}_5$ were created and models showed good agreement with the experimentally measured x-ray diffraction data. However, since the differences in $G(r)$ and $S(Q)$ are subtle, one must be careful in making sure that the errors in these functions are not greater than the difference between the as-deposited and annealed models. As deposited and annealed

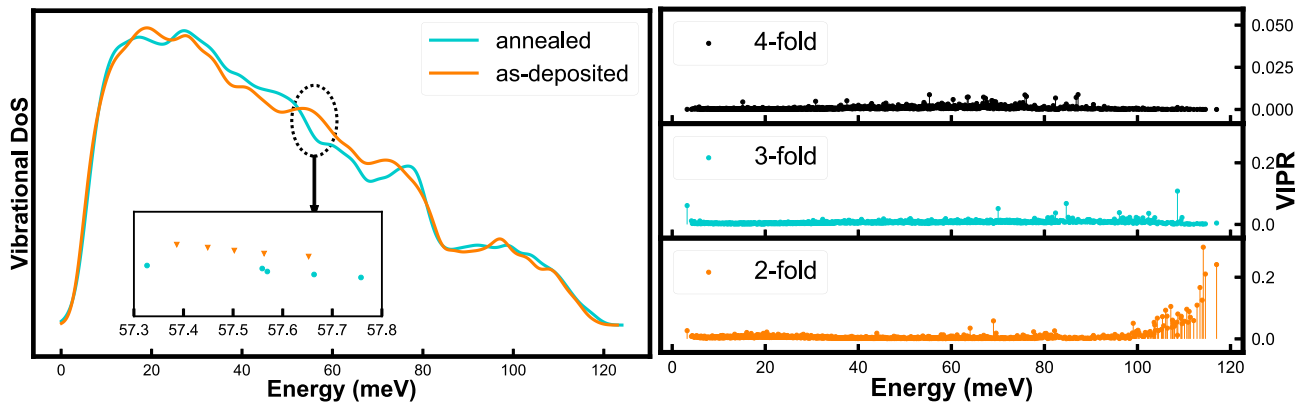


FIG. 11. Left panel: Vibrational density of states (arbitrary units) in as-deposited and annealed models. The insets show, in the energy range of interest, the energy associated with the normal modes in the as-deposited and annealed models. Right panel: Vibrational inverse participation ratio (VIPR), calculated for an as deposited model, projected onto different coordination of the O atoms.

models of zirconia-alloyed tantalum showed differences in structure in relation to the M–M correlations, coordination statistics, VR, void size, and distribution. Despite the subtle differences in the experimental x-ray diffraction data for as-deposited and annealed samples that manifests mostly in the polyhedral linking fashions, our models clearly capture them.

The effect of annealing on the coordination number is most prominent on the Ta atoms. Analysis of the VR showed that there is always an O atom closer to a void boundary than any metal atom. The void distribution highlights the presence of a greater number of larger voids in as-deposited models than in the annealed models. The electronic DOS shows that neither annealing nor zirconia doping significantly alters the band gap of the tantalum host. PBE functional calculations produce incorrect band gap for Zr-alloyed tantalum and the inclusion of hybrid functional for the DFT calculation is inevitable to get a good agreement with experimental results. The computa-

tional efficiency facilitated by FEAR helps us create 416-atom models, at DFT level, which would otherwise have been highly expensive using the traditional MQ method.

The results presented in this paper provide an increased understanding of the atomic structure of $\text{ZrO}_2:\text{Ta}_2\text{O}_5$ coatings and the effect of annealing on the structure—these results could be helpful to understand the origin of mechanical loss observed in these coatings so coatings with lower losses, as required by future generations of gravitational wave detectors, could be designed.

ACKNOWLEDGMENTS

This work used the Extreme Science and Engineering Discovery Environment (XSEDE), which is supported by National Science Foundation Grant No. ACI-1548562. We acknowledge the computational resources available to us through XSEDE under Allocation No. DMR-190008P.

- [1] M. Abernathy, A. Amato, A. Ananyeva, S. Angelova, B. Baloukas, R. Bassiri, G. Billingsley, R. Birney, G. Cagnoli, M. Canepa, M. Coulon, J. Degallaix, A. D. Michele, M. A. Fazio, M. M. Fejer, D. Forest, C. Gier, M. Granata, A. M. Gretarsson, E. M. Gretarsson *et al.*, *Classical Quantum Gravity* **38**, 195021 (2021).
- [2] G. Vajente, R. Birney, A. Ananyeva, S. Angelova, R. Asselin, B. Baloukas, R. Bassiri, G. Billingsley, M. M. Fejer, D. Gibson, L. J. Godbout, E. Gustafson, A. Heptonstall, J. Hough, S. MacFoy, A. Markosyan, I. W. Martin, L. Martinu, P. G. Murray, S. Penn *et al.*, *Classical Quantum Gravity* **35**, 075001 (2018).
- [3] K. Prasai, J. Jiang, A. Mishkin, B. Shyam, S. Angelova, R. Birney, D. A. Drabold, M. Fazio, E. K. Gustafson, G. Harry, S. Hoback, J. Hough, C. Lévesque, I. MacLaren, A. Markosyan, I. W. Martin, C. S. Menoni, P. G. Murray, S. Penn, S. Reid *et al.*, *Phys. Rev. Lett.* **123**, 045501 (2019).
- [4] M. Granata, E. Saracco, N. Morgado, A. Cajjfinger, G. Cagnoli, J. Degallaix, V. Dolique, D. Forest, J. Franc, C. Michel, L. Pinard, and R. Flaminio, *Phys. Rev. D* **93**, 012007 (2016).
- [5] S. D. Penn, P. H. Sneddon, H. A., J. C. Betzwieser, G. Cagnoli, J. Camp, D. R. M. Crooks, M. M. Fejer, A. M. Gretarsson, G. M. Harry, J. Hough, S. E. Kittelberger, M. J. Mortonson, R. Route, S. Rowan, and C. C. Vassiliou, *Classical Quantum Gravity* **20**, 2917 (2003).
- [6] G. M. Harry, M. R. Abernathy, A. E. Becerra-Toledo, H. Armandula, E. Black, K. Dooley, M. Eichenfield, C. Nwbugwu, A. Villar, D. R. M. Crooks, G. Cagnoli, J. Hough, C. R. How, I. MacLaren, P. Murray, S. Reid, S. Rowan, P. H. Sneddon, M. M. Fejer, R. Route *et al.*, *Classical Quantum Gravity* **24**, 405 (2007).
- [7] R. Flaminio, J. Franc, C. Michel, N. Morgado, L. Pinard, and B. Sassolas, *Classical Quantum Gravity* **27**, 084030 (2010).
- [8] A. Pandey, P. Biswas, and D. A. Drabold, *Sci. Rep.* **6**, 33731 (2016).
- [9] A. Pandey, P. Biswas, B. Bhattarai, and D. A. Drabold, *Phys. Rev. B* **94**, 235208 (2016).
- [10] B. Cai, X. Zhang, and D. A. Drabold, *Phys. Rev. B* **83**, 092202 (2011).

- [11] M. G. Tucker, D. A. Keen, M. T. Dove, A. L. Goodwin, and Q. Hui, *J. Phys.: Condens. Matter* **19**, 335218 (2007).
- [12] G. Kresse and J. Furthmüller, *Phys. Rev. B* **54**, 11169 (1996).
- [13] P. E. Blöchl, *Phys. Rev. B* **50**, 17953 (1994).
- [14] J. P. Perdew, K. Burke, and M. Ernzerhof, *Phys. Rev. Lett.* **77**, 3865 (1996).
- [15] H. Christiansen, M. Weigel, and W. Janke, *Phys. Rev. Lett.* **122**, 060602 (2019).
- [16] K. Prasai, R. Bassiri, H. P. Cheng, and M. M. Fejer, *Phys. Status Solidi B* **258**, 2000519 (2021).
- [17] A. K. Soper, *Neutron Scattering - Applications in Biology, Chemistry, and Materials Science*, edited by F. Fernandez-Alonso and D. L. Price, Experimental Methods in the Physical Sciences, Vol. 49 (Academic Press, Boston, 2017), pp. 135–211
- [18] J. Heyd, G. E. Scuseria, and M. Ernzerhof, *J. Chem. Phys.* **118**, 8207 (2003).
- [19] J. Heyd, G. E. Scuseria, and M. Ernzerhof, *J. Chem. Phys.* **124**, 219906 (2006).
- [20] A. V. Krukau, O. A. Vydrov, A. F. Izmaylov, and G. E. Scuseria, *J. Chem. Phys.* **125**, 224106 (2006).
- [21] J. Y. Tewg, Y. Kuo, and J. Lu, *Electrochem. Solid-State Lett.* **8**, G27 (2005).
- [22] B. Shyam, K. H. Stone, R. Bassiri, M. M. Fejer, M. F. Toney, and A. Mehta, *Sci. Rep.* **6**, 32170 (2016).
- [23] O. L. G. Alderman, C. J. Benmore, J. Neufeind, E. Coillet, A. Mermet, V. Martinez, A. Tamalonis, and R. Weber, *Phys. Rev. Materials* **2**, 043602 (2018).
- [24] N. Kim and J. F. Stebbins, *Chem. Mater.* **23**, 3460 (2011).
- [25] N. Kim and J. F. Stebbins, *J. Non-Cryst. Solids* **378**, 158 (2013).
- [26] C. H. Rycroft, *Chaos* **19**, 041111 (2009).
- [27] M. Gajdoš, K. Hummer, G. Kresse, J. Furthmüller, and F. Bechstedt, *Phys. Rev. B* **73**, 045112 (2006).
- [28] M. Fox, *Am. J. Phys.* **70**, 1269 (2002).
- [29] X. Wu, S. Soss, E. Rymaszewski, and T.-M. Lu, *Mater. Chem. Phys.* **38**, 297 (1994).
- [30] E. Bersch, S. Rangan, R. A. Bartynski, E. Garfunkel, and E. Vescovo, *Phys. Rev. B* **78**, 085114 (2008).
- [31] R. Thapa, B. Bhattarai, M. N. Kozicki, K. N. Subedi, and D. A. Drabold, *Phys. Rev. Materials* **4**, 064603 (2020).
- [32] J. P. Perdew, *Int. J. Quantum Chem.* **28**, 497 (1985).
- [33] J. Y. Kim, B. Magyari-Köpe, K. J. Lee, H. S. Kim, S. H. Lee, and Y. Nishi, *Phys. Status Solidi RRL* **8**, 560 (2014).
- [34] J. Li, S. Meng, J. Niu, and H. Lu, *Journal of Advanced Ceramics* **6**, 43 (2017).
- [35] K. Aryana, D. A. Stewart, J. T. Gaskins, J. Nag, J. C. Read, D. H. Olson, M. K. Grobis, and P. E. Hopkins, *Nat. Commun.* **12**, 2817 (2021).
- [36] B. Li, F. DeAngelis, G. Chen, and A. Henry, *Normal Mode Analysis of The Thermal conductivity in Amorphous Polymers: The Importance of Localized Modes* (Research Square, 2021).